A&A 534, A119 (2011)
DOI: 10.1051/0004-6361/201117684

Astronomy & Astrophysics

Overview of an extensive multi-wavelength study of GX 339−4 during the 2010 outburst

M. Cadolle Bel[1], J. Rodriguez[2], P. D'Avanzo[3], D. M. Russell[4], J. Tomsick[5], S. Corbel[2], F. W. Lewis[6], F. Rahoui[7], M. Buxton[8], P. Goldoni[9], and E. Kuulkers[1]

[1] ESAC, ISOC, Villañueva de la Cañada, Madrid, Spain
e-mail: Marion.Cadolle@sciops.esa.int
[2] Laboratoire AIM, UMR 7158, CEA/DSM – CNRS – Université Paris Diderot, IRFU/SAp, Gif-sur-Yvette, France
[3] INAF, Osservatorio Astronomico di Brera, Merate, Italy
[4] University of Amsterdam (Anton Pannekoek Institute), The Netherlands
[5] SSL/California University, Berkeley, USA
[6] Faulkes Telescope Project, University of Glamorgan, Wales, UK
[7] Astronomy Department, Harvard University & Harvard-Smithsonian Center for Astrophysics, Cambridge, USA
[8] Astronomy Department, Yale University, USA
[9] Laboratoire APC, UMR 7164, CEA/DSM – CNRS – Université Paris Diderot, IRFU/SAp, Paris, France

Received 11 July 2011 / Accepted 20 September 2011

ABSTRACT

Context. The microquasar GX 339−4 experienced a new outburst in 2010: it was observed simultaneously at various wavelengths from radio up to soft γ-rays. We focus on observations that are quasi-simultaneous with those made with the INTEGRAL and RXTE satellites: these were collected in 2010 March–April during our INTEGRAL target of opportunity programme, and during some of the other INTEGRAL observing programmes with GX 339−4 in the field-of-view.
Aims. X-ray transients are extreme systems that often harbour a black hole, and are known to emit throughout the whole electromagnetic spectrum when in outburst. The goals of our programme are to understand the evolution of the physical processes close to the black hole and to study the connections between the accretion and ejection.
Methods. We analysed radio, NIR, optical, UV, X-ray and soft γ-ray observations. We studied the source evolution in detail by producing light curves, hardness-intensity diagrams and spectra. We fitted the broadband data with phenomenological, then physical, models to study the emission coming from the distinct components.
Results. Based on the energy spectra, the source evolved from the canonical hard state to the canonical soft state. The source showed X-ray spectral variations that were correlated with changes in radio, NIR and optical emission. The bolometric flux increased from 0.8 to 2.9×10^{-8} erg cm^{-2} s^{-1} while the relative flux and contribution of the hot medium decreased on the average. Reprocessing in the disc was likely to be strong at the end of our observations.
Conclusions. The source showed a behaviour similar to that of previous outbursts, with some small deviations in the hard X-ray parameter evolution. The radio, NIR and optical emission from jets was detected and observed to fade as the source softened. The results are discussed within the context of disc and jet models.

Key words. black hole physics – stars: individual: GX 339−4 – gamma rays: general – X-rays: binaries – infrared: general – radio continuum: general

1. Introduction

X-ray transients (XTs) are accreting low-mass X-ray binaries (LMXBs) that spend most of their time in a faint, quiescent state. They undergo large amplitude outbursts with rise times of only a few days or weeks (or months in the case of GX 339−4), with typical recurrence periods of many years (Tanaka & Shibazaki 1996). It is commonly accepted that the outburst of an XT is the result of an accretion disc instability (Frank et al. 2002). This process triggers a transition from a quiescent state with a very low mass accretion rate ($\dot{m} \ll 0.01\ \dot{M}_{\rm Edd}$), where the source activity is very faint or undetected (luminosity $\leq 10^{33}$ erg s^{-1}), to active states. During outbursts, the optically thick and geometrically thin accretion disc has a varying inner radius (e.g., Tomsick et al. 2009) and temperature, emitting at typical X-ray energies of ∼1 keV. The inner regions of the disc (and the compact object) are embedded in a hot and tenuous medium often referred to as the corona, where soft X-ray photons originating in the disc undergo inverse Comptonisation. This results in a power-law spectrum that has been detected up to a few MeV in some sources (Grove et al. 1998; Zdziarski et al. 2004; Cadolle Bel et al. 2006; Laurent & Titarchuk 2007). The exact origin of this high-energy power-law spectrum is, however, subject to debate, and part of the high-energy emission could instead arise from synchrotron emission from a relativistic jet, which is usually seen in the radio domain (Markoff et al. 2005). Note that Laurent et al. (2011) recently showed, through the discovery of polarized γ-ray emission, that both inverse Comptonisation and synchotron emission explained the 20 keV to ∼2 MeV spectrum of the persistent X-ray binary Cygnus X-1.

The spectral characteristics are coupled with different levels of variability, quasi periodic oscillations (QPOs) observed in the power density spectrum (PDS) (e.g., Belloni et al. 2001, 2005) and with the properties of the jet emission at radio, optical and

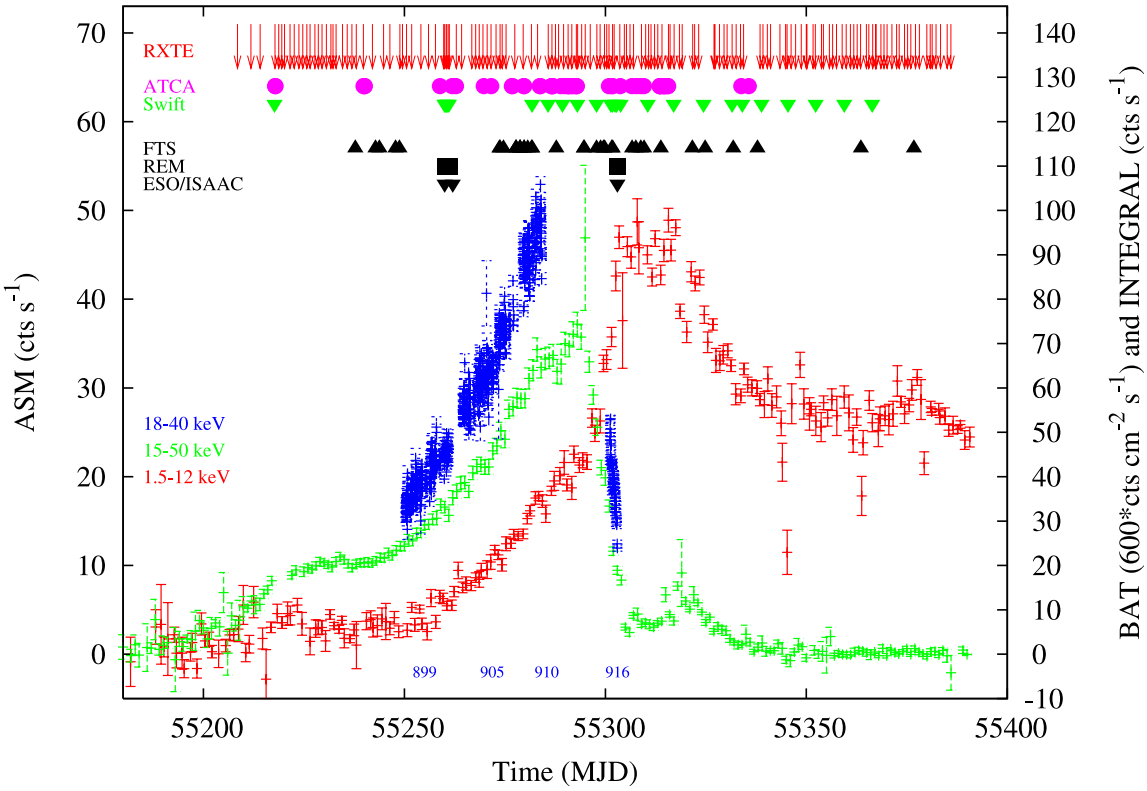

Fig. 1. Daily RXTE/ASM (red), *Swift*/BAT (green) and INTEGRAL/ISGRI (per pointing, violet) light curves of GX 339−4 during the 2010 outburst. Other observations performed with ATCA, the FTS, the REM/ROSS, REMIR and the ESO/ISAAC telescopes are indicated. The blue numbers near the bottom of the figure are INTEGRAL revolution numbers (see Table 1 for details).

IR frequencies (see, e.g., Russell et al. 2006; Coriat et al. 2009). Based on the relative strengths of each spectral component, the degree of variability and shape of the PDS and on the properties of the radio emission, different spectral states have been defined (e.g., McClintock & Remillard 2006; Homan & Belloni 2005). The two main canonical spectral states are the low/hard state (LHS) and the high/soft state (HSS). The X-ray energy spectrum in the LHS is dominated by hard power-law-like emission and the PDS shows a high level of variability dominated by a strong (∼30% fractional rms) band-limited noise, associated with the presence of low-frequency QPOs. The LHS exhibits a continuously launched compact jet, whose radio-spectrum is flat (Corbel et al. 2000, 2003; Gallo et al. 2003, 2006; Fender et al. 2004). Thermal emission from the disc dominates the spectrum in the HSS, and the PDS shows only a weak power-law noise component. No core radio emission is detected, and radio detections made during the HSS are likely to originate in discrete ejections that were launched previously (see, e.g., Fender et al. 2009). Other states have been identified and both are intermediate flavours of the canonical ones. These are the HIMS (hard intermediate state) and SIMS (soft intermediate state) as defined in Belloni (2010).

GX 339−4 is a recurrent XT with regular outbursts, shown to be a ∼7-solar-mass black hole (BH) from dynamical studies (Hynes et al. 2003; Muñoz-Darias et al. 2008) with well-sampled X-ray (e.g., Belloni et al. 2005) and multi-wavelength coverage during outbursts (e.g., Corbel et al. 2000; Homan et al. 2005; Coriat et al. 2009). On January 3, 2010, GX 339−4 entered a new outburst (Yamaoka et al. 2010). We triggered INTEGRAL during the initial hard X-ray phase (Tomsick 2010; Prat et al. 2010); subsequently, we triggered the second part of our INTEGRAL campaign on GX 339−4 (see Fig. 1) in its declining hard X-ray phase (Cadolle Bel et al. 2010). The source increased in intensity in soft X-rays while it kept declining in hard X-rays (as announced in Shaposhnikov & Tomsick 2010; Yu 2010), exiting the LHS (Buxton et al. 2010) towards a softer state.

Here, we report the results of our INTEGRAL observations of GX 339−4 together with *Swift*, RXTE and UV/optical/NIR/radio data. We start with a description of the available data and of the analysis procedures employed in Sect. 2. Results are presented in Sect. 3, followed by their interpretations and modelling in Sect. 4. We summarize our studies in Sect. 5.

2. Observations and data reduction

Table 1 summarizes the observations analysed in this paper, providing instrument details, energy ranges, dates, and modes. Figure 1 shows the RXTE/ASM, *Swift*/BAT X-ray and INTEGRAL light curves of the outburst, with the time of the other multi-wavelength observations indicated.

2.1. INTEGRAL

Target of opportunity observations (ToO) were performed during MJD 55259–55261 and 55301–55303, corresponding to revolutions # 902 and # 916, respectively (hereafter, Rev.: an INTEGRAL orbit around the Earth lasts ∼3 days). We also used data from INTEGRAL programmes of observations of the Galactic Bulge (Kuulkers et al. 2007), RX J1713.7-3946 and the Galactic disc (performed between MJD 55237–55285, Rev. # 895–910).

The IBIS/ISGRI and JEM-X data were reduced using standard analysis procedures of the off-line scientific analysis

Table 1. Log of the GX 339−4 observations analysed in this paper.

Observatory	Instrument	Bandpass	Period (MJD−55000)	Observation Type
INTEGRAL[a]	IBIS/ISGRI	18–200 keV	237.5–303.3	ToO (5 × 5[b] , Hex[c])
	JEM-X	5–25 keV	237.5–303.3	ToO
RXTE[a]	PCA	3–25 keV	208.5–345.4	Public
Swift[d]	XRT	0.3–10 keV	217.7–352.3	Public
	BAT	20–100 keV	217.7–352.3	Public
	UVOT	180–600 nm	217.7–352.3	Public
REM[d]	ROSS, REMIR	550–2159 nm	260.2–261.4 and 303	ToO
FTS[d]	Merope	460–883 nm	237.7–337.8	Public
ATCA[d]	–	5.5–9 GHz	261–263	ToO

Notes. [(a)] Interrupted observations: almost all Rev. (∼3 days) between # 895–916 for INTEGRAL; Galactic Bulge monitoring for RXTE. [(b)] 5 × 5 dither pattern around the nominal target location. [(c)] Hexagonal pattern around the nominal target location. [(d)] Snap-shot observations with the specified instruments or receivers.

`OSA 9.0` following standard procedures (e.g., Rodriguez et al. 2008; Cadolle Bel et al. 2009) for the production of images, spectra and light curves. Systematic errors of 2% were added for both JEM-X (in the 5–25 keV range) and ISGRI (in the 18–400 keV range). We used the maps, the response matrices and the off-axis and background corrections from `OSA 9.0`. We checked that the spectral index did not change by more than 2% during a single revolution by carrying out spectral analysis for each pointing. The low level of spectral variation over a single revolution allowed us to average all spectra belonging to the same revolution, which improved the signal-to-noise ratio. The ISGRI light curves are shown in Figs. 1 and 2 (fourth panel down). We were only able to perform JEM-X analysis on our ToO data because the source was outside the field-of-view (FOV) of JEM-X in the other programmes. Because the RXTE/PCA instrument observed the source more frequently and had a higher sensitivity than JEM-X, the JEM-X data were not included in the broad-band spectra to be consistent over all our data sets. However, we verified that the best-fit spectral parameters using JEM-X and PCA were consistent within the error bars.

2.2. RXTE

We analysed all available observations, taken about once every two days from MJD ∼ 55217 to 55311. Each observation lasted between ∼1 and 5 ks. The RXTE data were reduced with the `HEASOFT` software package v6.10, following standard procedures (see Rodriguez et al. 2008). Energy spectra were only extracted from the top layer of the PCA detector 2. We used the latest calibration files provided by the RXTE guest observer facility. A level of 0.6% systematic error was adopted for GX 339−4 to account for uncertainties in the PCA response (Jahoda et al. 2006). The resultant RXTE/PCA spectra of a single observation were fitted simultaneously between 3–25 keV. Note that we also added the IBIS/ISGRI data when available; one INTEGRAL revolution corresponds typically to three distinct RXTE observations (we checked that the spectral parameters were not changing significantly and could be averaged). The ASM and PCA light curves are shown in Fig. 2 (first and second panels down).

2.3. Swift

All *Swift*/XRT observations discussed in this paper were made in window timing (WT) mode to avoid pile-up due to the source brightness. Level 2 event files were produced following standard processing and screening procedures with `xrtpipeline` (v0.12.6). The source- and background spectra were then extracted from these files within `xselect` from the grade 0 events only. Source spectra were obtained within a 40-pixel diameter circle centred on the source position, while background spectra were obtained using a similar sized region at an off-axis position. An ancillary response file taking into account the exposure map of the observation was generated for each spectrum

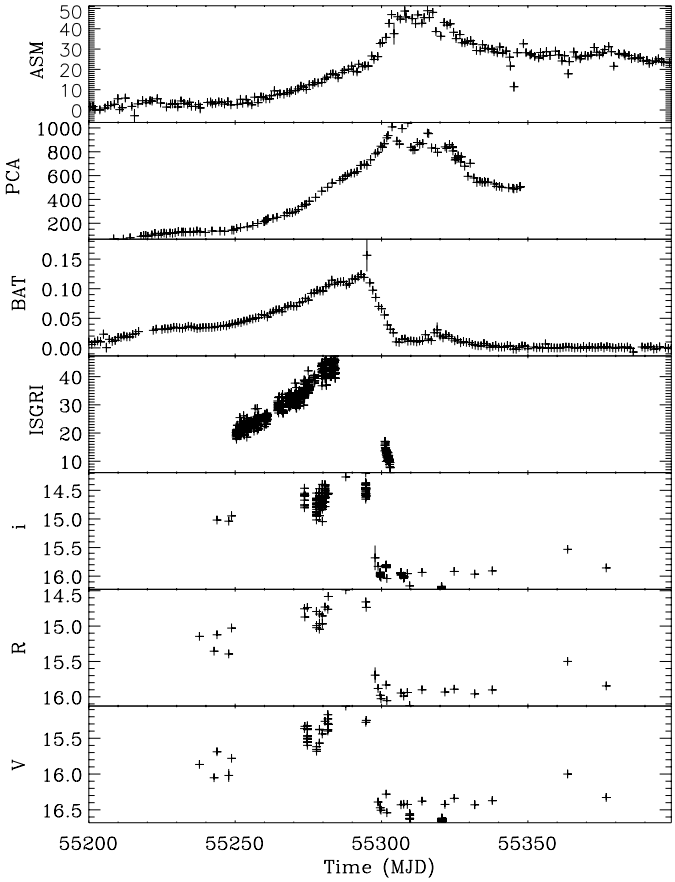

Fig. 2. RXTE/ASM (cts s^{-1} in 1.5–12 keV), PCA (cts s^{-1} in 3–30 keV), *Swift*/BAT (cts cm^{-2} s^{-1} in 15–50 keV), INTEGRAL/ISGRI (cts s^{-1} in 40–80 keV) and FTS light curves (filters V, R and i') obtained from MJD 55200 to 55400.

with `xrtmkarf`, and the latest version of the redistribution matrix file was used in the fitting process. The original spectra were rebinned by a factor of 4 before the fitting process. Additionally, the BAT light curve (publicly available on-line) is shown in Figs. 1 and 2 (third panel down).

In addition, data were collected from the *Swift*/UVOT (UV and optical) instrument, with MJD spanning from 55217 to 55310 simultaneously with INTEGRAL. The six UVOT filters span the wavelength range 1800–6000 Å. The camera has a $17' \times 17'$ FOV, resulting in images of 2048×2048 pixels (Roming et al. 2005). The UVOT images were combined using the standard UVOT `uvotimsum` routine and magnitudes calculated using the `uvotsource` command as provided by HEASARC using an aperture of $6''$ (see Poole et al. 2008). Detections (at a significance of 3σ) are discussed in Sect. 4.

2.4. REM and FTS

Optical and NIR observations were performed with the REM (rapid eye mounting) telescope (see, e.g., Zerbi & The Rem Team 2001; Chincarini et al. 2003; Covino et al. 2004) equipped with the ROSS optical spectrograph/imager and the REMIR NIR camera. Observations of GX 339-4 were carried out around MJD 55260.3, 55261.3 and 55303.3. Image reduction was carried out by following standard procedures: subtraction of an averaged bias frame and division by a normalized flat frame. Astrometry was performed using the USNOB1.0[1] and the 2MASS[2] catalogues. Aperture photometry was performed with the SExtractor package (Bertin & Arnouts 1996) for all objects in the field to analyse the REM data. The calibration was made against Landolt standard stars for the optical filters and against the 2MASS catalogue for NIR filters. To minimize any systematic effect, we performed differential photometry with respect to a selection of local isolated and non-saturated standard stars.

Optical data were also collected using the 2-m robotic Faulkes Telescope South (FTS) located at Siding Spring, New South Wales, Australia, using the Merope camera (EM03) coupled with an E2V CCD42-40DD CCD. This produces a $4\farcm7 \times 4\farcm7$ FOV and images of 2048×2048 pixels binned 2×2 to give 1024×1024 pixels at 0.278 arcsec pixel^{-1}. Science images were produced using an automatic pipeline that de-biases and flat-fields the raw images[3]. Generally, 200 s exposures were acquired in each of the Bessel-V, Bessel-R and SDSS-i' filters, approximately weekly as part of a long-term monitoring campaign on GX 339−4 and 34 other LMXBs (Lewis et al. 2008). On some dates, multiple images were taken (mostly in the i' band) to investigate variability on minute-timescales. Seeing values range from $0\farcs8$ to $3\farcs2$. Images were discarded if the signal-to-noise ratio was low (often due to thin cloud), or if the tracking or focus were poor. In total, there are 338 usable images taken within the time range of interest. We performed aperture photometry of GX 339−4 and four nearby field stars using APPHOT in IRAF. In addition, we used a non-variable star, which was fainter or of similar magnitude to GX 339−4 to assess its level of variability. A fixed aperture radius of 6 pixels along with a background annulus of 10–20 pixels was adopted for all stars in all filters. Flux calibration in V, R and i' bands was achieved using photometry of the standard star field RU 149, from the list of Landolt photometric stars (Landolt 1992), which are observed regularly by FTS. We used the stars A, B, C, D, and F as catalogued in the star field RU 149. The i' magnitudes of the stars in the RU 149 field were estimated from the known R- and I- band magnitudes using the conversion of Jordi et al. (2006). Uncertainties were calculated from the range of measurements from the RU 149 field stars (5 stars × 2 per filter = 10 measurements per filter). We used the small differences between our measurements and these reported measurements to apply a small correction to the V, R and i' calibration of the GX 339−4 field stars to achieve a more accurate calibration. The FTS light curves are shown in Fig. 2 (lower three panels).

[1] http://www.nofs.navy.mil/data/fchpix/

[2] http://www.ipac.caltech.edu/2mass/

[3] http://telescope.livjm.ac.uk/Info/TelInst/Inst/RATCam/#pipe

2.5. Radio

GX 339−4 was frequently observed at radio frequencies with the Australia Telescope Compact Array (ATCA) and the new CABB back-end. ATCA observed the source several times (PI Corbel) during the outburst. We concentrated on the simultaneous observations gathered with INTEGRAL and ground-based instruments at MJD 55261.89 and 55262.91. Fluxes were 9.02 ± 0.10 mJy, 9.56 ± 0.05 mJy then 8.16 ± 0.05 mJy and 7.94 ± 0.10 mJy at, respectively, 5.5 and 9.0 GHz.

3. Results

The following sub-sections refer to the X/γ-ray, UV, optical and NIR light curves shown in Fig. 2 as well as to the HID (Fig. 3) and radio data. Some spectra are shown in Figs. 4 and 5.

3.1. Light curves

Figure 2 presents the light curves obtained with the ASM (2–10 keV), PCA (3–30), BAT (15–40 keV), ISGRI (40–80 keV) and FTS (V, R and i' magnitudes) instruments. The source shows the typical behaviour of an XT: the outburst started in hard X-rays probably around MJD ∼ 55199. The light curve morphologies at the peak of BAT and ASM are quite different. The hard X-rays dropped before the soft X-ray peak: around MJD 55295, the hard X-rays reached their peak and the emission began to decrease (with a secondary peak at MJD 55319) while the source continued to increase in soft X-rays until MJD 55327 (i.e., more than a month later), before decreasing. This behaviour indicates a state transition from a hard to a softer state. The optical (e.g., Fig. 2) also dropped at the start of the transition, as reported in previous outbursts of GX 339−4 (Homan et al. 2005; Coriat et al. 2009).

While during MJD 55259.9–55261.1 (Rev. # 902) the source was still in a hard state, during MJD 55301.1–55303.3 (Rev. # 916) GX 339−4 was extremely bright in the *Swift*/XRT (>400 cts s^{-1}) instrument. The JEM-X fluxes were around 370 mCrab and 240 mCrab in, respectively, the 3–10 and 10–20 keV energy bands, while the ISGRI fluxes were varying around 190 mCrab and 130 mCrab in the 20–40 keV and 40–80 keV energy bands. These numbers show that the X-ray source was softening.

3.2. Hardness intensity diagram

To study the X-ray spectral and flux evolution during the outburst, we produced a hardness-intensity diagram (HID) with *RXTE*/PCA (Fig. 3) similar to those widely used in the literature (e.g., Fender et al. 2004). There was no *INTEGRAL* coverage from the start of the outburst to the peak, hence we

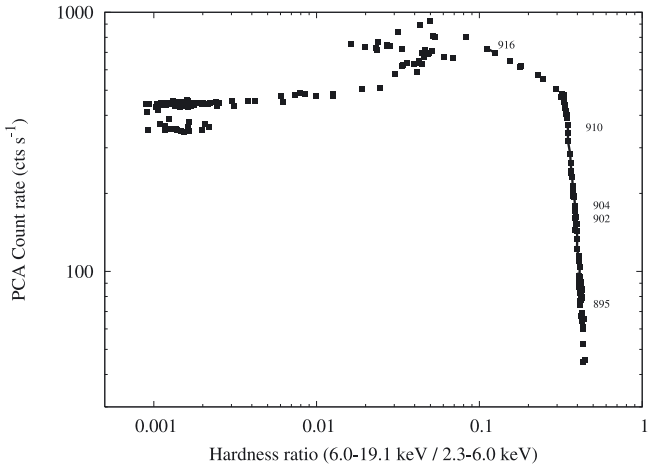

Fig. 3. HID of GX 339–4 (logarithmic scale) obtained with the top layer of RXTE/PCA (2.3–19.1 keV, detector 2) between MJD 55208 and 55347 (the numbers indicate some of the INTEGRAL revolutions). The source generally evolves from bottom to top, and from right to left.

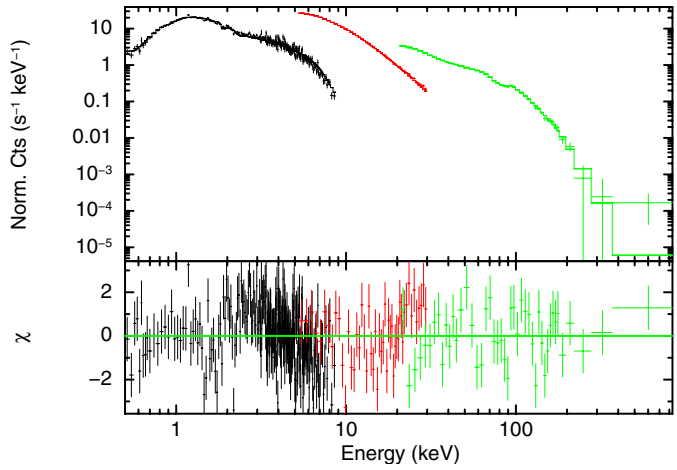

Fig. 4. *Swift*/XRT (black), RXTE/PCA (red) and INTEGRAL/ISGRI (green) LHS count rate spectra of GX 339-4 (first ToO of March 2010, Rev. # 902, MJD ∼ 55259.9–55261.1) fitted with an absorbed multicolour disc, reflection, Fe line and Comptonisation components.

focused on the main part of the outburst simultaneously with our INTEGRAL data. The HID extends slightly beyond the main data log analysed in this paper, to illustrate the evolution of the source after our campaign). GX 339–4 followed the usual path of XTs in outburst on this diagram (see, e.g., Belloni et al. 2005), with some small deviations in the usual track.

3.3. X-ray and γ-ray spectra

We fitted the closest (in time) XRT (0.5–9.2 keV, when available), PCA (3–30 keV) and IBIS/ISGRI (18–200 keV) spectra simultaneously with `XSPEC v12.6.0` (Arnaud 1996). Several models were tested when analysing the spectra. A normalization constant was added to account for uncertainties in the cross-calibration of the instruments. The data were in general well-fitted using absorbed power-law (or cut-off power-law and Comptonisation) with reflection combined with a multicolour black-body, and a Gaussian at ∼6.5 keV attributed to a fluorescent iron (Fe) line. We were unable to constrain the line centroid well with the PCA: we therefore fixed the energy of the line to lie between ∼6 keV and 7.5 keV. An additional line at

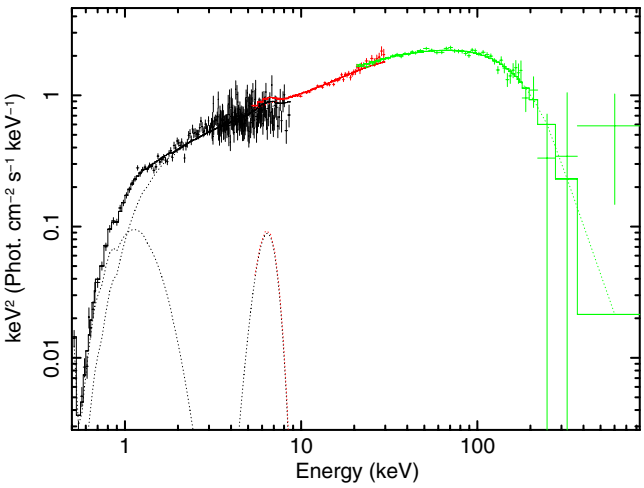

Fig. 5. Same as Fig. 4, but in distinct units: keV^2 × Photons cm^{-2} s^{-1} keV^{-1}.

2 keV (caused by calibration problems) was sometimes needed in XRT. Absorption was a combination of a fixed interstellar component (abundances fixed to Wilms et al. 2000) plus a variable local component. XRT found the total absorption to vary between 4.9–6.3 × 10^{21} cm^{-2}, taking into account the statistical uncertainties (±0.07), and the dependence on the position of the source in the HID. The lower end (4.9 × 10^{21} cm^{-2}) is compatible, within the errors, with the average Galactic column density in the source direction estimated from Kalberla et al. (2005); it is possible that up to about 1.4 × 10^{21} cm^{-2} is intrinsic and variable (see Cabanac et al. (2009) for a detailed discussion of the variations of the absorption in this source; XRT data were not always available to do that in this work). For the disc component, the DISKBB model in `XSPEC` (Mitsuda et al. 1984) was used. We then replaced the phenomenological models, which had at first allowed us to easily compare the spectral parameters over the outburst, with a more physical one, the thermal Comptonisation model of Titarchuk (1994). We tested the best modelling by adding additional contributions and we carefully checked any improvement in the goodness of the fit. When a cut-off was needed, this provided a good fit to almost all our data (see Tables 2 and 3 for details; otherwise, we used a simple power-law model), although the temperature of the seed photons (tied to the disc temperature) was not always well constrained.

The best-fit parameters are reported in Table 2; Table 3 shows the phenomenological cut-off power-law parameters. In addition to providing a more physical interpretation to the data, this model also permits us to avoid the divergence of the power law flux towards low energy because Comptonisation significantly contributes above 3× $kT_{\rm in}$, and decreases significantly below this energy. Our spectral fitting in general led to normalization constants very close to 1 for all instruments. Examples of the fitted spectra obtained during our INTEGRAL observations are shown in counts in Fig. 4 with residuals, and in Fig. 5 in energy units (keV^2 × Photons cm^{-2} s^{-1} keV^{-1}). A small excess was seen at high energies, but a non-thermal modelling did not improve our fits: this excess was not significant. A plot summarizing the main spectral parameters for all observations is shown in Fig. 6. Large error bars correspond to poorly constrained data.

Apart from three very low values around MJD 55217, 55260 and 55280, the disc temperature values were remarkably constant, around 0.6–0.8 keV, until the source transited to a softer state. After the transition, the disc temperature was first found

Table 2. Best-fit spectral parameters around the period of our main *INTEGRAL* observations.

Time (MJD[a])	Observations (Rev. #)	Disc Norm.[b]	$kT_{\rm in}$ (keV)	$kT_{\rm e}$ (keV) or Γ	τ[c]	$E_{\rm Fe}$ line (keV)	$\omega^d/2\pi$	$\chi^2_{\rm red}$ (d.o.f.)	F^e	$F_{\rm bol}{}^f$
217.7–217.8	N.A.[g]	33784^{+28803}_{17644}	0.18 ± 0.01	$\Gamma = 1.62 \pm 0.02$	–	$6.53^{+0.32}_{-0.35}$	$0.34^{+0.10}_{-0.08}$	1.45 (281)	1.43	N.A.
237.5–240.2	895[h]	35^{+20}_{-9}	0.83 ± 0.10	41^{+5}_{-4}	$1.63^{+0.14}_{-0.17}$	$6.56^{+0.20}_{-0.25}$	0.25 ± 0.05	0.84 (97)	1.99	0.82
240.7–243.2	896[h]	100^{+186}_{-50}	$0.67^{+0.02}_{-0.11}$	38^{+4}_{-3}	$1.69^{+0.13}_{-0.14}$	$6.15^{+0.21}_{-0.15}$	$0.19^{+0.05}_{-0.04}$	1.05 (102)	2.19	0.89
243.7–246.2	897[h]	100 ± 50	0.65 ± 0.10	41^{+5}_{-3}	$1.53^{+0.12}_{-0.15}$	$6.00_i{}^{+0.14}$	0.21 ± 0.03	1.13 (103)	2.14	0.86
246.7–249.1	898[h]	100^{+91}_{-50}	$0.64^{+0.03}_{-0.07}$	39^{+6}_{-3}	$1.59^{+0.14}_{-0.15}$	$6.00_i{}^{+0.25}$	0.22 ± 0.05	1.14 (102)	2.29	0.92
249.7–252.1	899[h]	66^{+252}_{-29}	$0.75^{+0.14}_{-0.20}$	40^{+5}_{-3}	$1.59^{+0.13}_{-0.15}$	6.37 ± 0.20	0.26 ± 0.05	1.09 (102)	2.49	1.02
252.5–255.1	900[h]	102 ± 51	$0.68^{+0.13}_{-0.19}$	39^{+4}_{-3}	$1.59^{+0.13}_{-0.15}$	$6.17^{+0.23}_{-0.49}$	$0.25^{+0.05}_{-0.04}$	0.78 (102)	2.74	1.09
255.6–258.1	901[h]	124^{+388}_{-56}	$0.70^{+0.11}_{-0.16}$	45^{+7}_{-4}	$1.36^{+0.14}_{-0.17}$	$6.31^{+0.30}_{-0.70}$	0.32 ± 0.04	0.99 (102)	3.18	1.25
259.9–261.1	902	82887^{+63704}_{-38606}	0.19 ± 0.01	38^{+3}_{-2}	$1.49^{+0.10}_{-0.11}$	$6.23^{+0.15}_{-0.23}$	0.25 ± 0.04	1.58 (333)	3.38	1.64
264.5–267.1	904[h]	134^{+441}_{-57}	$0.73^{+0.12}_{-0.18}$	39^{+4}_{-3}	$1.45^{+0.11}_{-0.13}$	$6.23^{+0.29}_{-0.66}$	$0.34^{+0.05}_{-0.04}$	1.07 (102)	4.21	1.51
267.6–270.1	905[h]	183^{+1406}_{-87}	$0.67^{+0.12}_{-0.20}$	41^{+5}_{-3}	$1.31^{+0.12}_{-0.14}$	$6.27^{+0.27}_{-0.70}$	0.35 ± 0.04	1.11 (102)	4.60	1.61
270.4–272.8	906[h]	370^{+1664}_{-199}	$0.60^{+0.11}_{-0.13}$	38^{+4}_{-3}	$1.40^{+0.11}_{-0.12}$	$6.07^{+0.30}_{-0.47}$	$0.32^{+0.04}_{-0.03}$	1.33 (102)	5.04	1.77
273.4–276.0	907[h]	198^{+568}_{-71}	$0.68^{+0.09}_{-0.15}$	39^{+4}_{-3}	$1.28^{+0.11}_{-0.13}$	$6.45^{+0.19}_{-0.50}$	$0.35^{+0.05}_{-0.04}$	1.59 (102)	5.67	1.98
276.4–278.8	908[h]	338^{+2463}_{-174}	$0.62^{+0.13}_{-0.17}$	37^{+4}_{-3}	$1.28^{+0.11}_{-0.13}$	$6.29^{+0.35}_{-0.65}$	0.39 ± 0.06	1.15 (102)	6.59	2.15
279.4–281.5	909	32816^{+33761}_{-19118}	$0.21^{+0.02}_{-0.01}$	39^{+4}_{-3}	$1.16^{+0.11}_{-0.13}$	$6.23^{+0.15}_{-0.25}$	0.39 ± 0.04	0.88 (312)	7.80	2.79
281.7–281.8	N.A.[g]	52^{+24}_{-20}	0.85 ± 0.09	$\Gamma = 1.80 \pm 0.01$	–	$6.27^{+0.16}_{-0.22}$	0.38 ± 0.06	0.57 (255)	7.94	N.A.
282.4–284.9	910[h]	32^{+23}_{-6}	$1.19^{+0.10}_{-0.11}$	40^{+4}_{-3}	1.14 ± 0.12	$6.00_i{}^{+0.58}$	0.49 ± 0.04	0.96 (96)	7.69	2.25
289.3–289.6	N.A.[g]	$840436^{+118692}_{-505374}$	$0.16^{+0.02}_{-0.01}$	$\Gamma = 1.79 \pm 0.03$	–	$6.14^{+0.21}_{-0.29}$	0.28 ± 0.07	1.34 (228)	9.65	N.A.
297.8–297.9	N.A.[g]	174096^{+86620}_{-62284}	0.22 ± 0.01	$\Gamma = 1.95 \pm 0.02$	–	$6.00_i{}^{+0.04}$	0.10 ± 0.05	1.32 (260)	11.4	N.A.
301.1–303.3	916	3196^{+367}_{-288}	0.61 ± 0.02	256^{+6}_{-83}	$0.01^{+0.02}_{-0.01}$	$6.00_i{}^{+0.22}$	$0.51^{+0.09}_{-0.10}$	1.91 (252)	12.2	2.93
303.6–303.8	N.A.[g]	2652^{+526}_{-353}	0.73 ± 0.04	35^{+5}_{-14}	$0.50^{+0.28}_{-0.50}$	$6.74^{+0.16}_{-0.14}$	$0.36^{+0.44}_{-0.32}$	1.77 (192)	14.6	N.A.
310.6–310.7	N.A.[g]	999^{+45}_{-44}	$1.00^{+0.02}_{-0.01}$	$\Gamma = 2.33^{+0.06}_{-0.07}$	–	$6.15^{+0.08}_{-0.09}$	–	1.50 (178)	13.3	N.A.

Notes. Models applied in XSPEC notations: CONSTANT*PHABS*REFLECT*(DISKBB+GAUSSIAN+POWERLAW) or CONSTANT*PHABS*REFLECT*(DISKBB+GAUSSIAN+COMPTT) (not all components always needed). Γ is the photon index. $N_{\rm H}$ varied between 4.9–6.3 $\times 10^{21}$ cm^{-2}. Errors are given at the 90% confidence level ($\Delta\chi^2 = 2.7$). [a] MJD−55000. [b] Disc normalization K is proportional to $(R/D)^2 \cos\theta$, where R is the inner disc radius in km, D is the distance to the source in kpc and θ the inclination angle of the disc. [c] Plasma optical depth. [d] Reflection scaling factor (1 for isotropic source above disc). [e] Computed in the 2–20 keV range. Units: 10^{-9} erg cm^{-2} s^{-1}. [f] X-ray bands extrapolated in the 0.01 keV–10 MeV range. Units: 10^{-8} erg cm^{-2} s^{-1}. [g] N.A. = Non Applicable (only XRT and PCA data available). [h] XRT data not available. [i] Pegged at lower limit (6 keV).

at its lowest values, but it returned to its pre-transition value (by MJD 55302) within a time frame of about 10–12 days, even though the power-law index continued to increase (see next paragraph). The observed inner disc temperature and the normalization evolution, which could be high (up to MJD ∼ 55303, Rev. #916) before decreasing (see Table 2), correspond to what is usually observed for GX 339−4 in outburst (see Sect. 4.1). The radius inferred from DISKBB is questionable, however (Gierliński et al. 2008). Several corrections need to be applied (colour correction factor, irradiation of the disc distorting the spectrum, physical prescription for the inner boundary condition), but these have large uncertainties. Moreover, the size of the correction can vary with time. Therefore, we only show the fraction of the flux in Fig. 6 that is in the DISKBB component with respect to the power-law flux: as expected, its contribution increased with time. The reflection component also evolved accordingly: its contribution increased with time, from 0.19 to 0.51, compatible with the source moving towards a softer state.

From MJD 55217 to 55311, the power-law photon index varied between 1.6 and 2.4 (or a cut-off power-law between 1.3–2.3, Table 3). In the early stages of the outburst, a cut-off is needed in the spectral fits (the Comptonisation model improves the $\chi^2_{\rm red}$), whereas it disappears in the softer states. Indeed, later data are better fitted with a simple power-law model (Table 2). This indicates a cooling of the corona as the thermal component gets stronger, and then a change of the emission mechanism at the state transition. This further confirms that the source made a transition from a hard to soft state. With the model of Titarchuk (1994), we obtained temperatures ($kT_{\rm e}$) and optical depth (τ) values before Rev. # 916 that yield a Comptonisation parameter ($y \times m_{\rm e}c^2$) of 0.10–0.22, typical for a BH in the rising phase of the LHS. The bolometric flux extrapolated between 0.01 keV and 10 MeV (note that the bulk of emission is between 0.1 and 100 keV) rose from 0.8 to 2.9 $\times 10^{-8}$ erg cm^{-2} s^{-1} while the 2–20 keV flux rose from 1.4 to 14.6 $\times 10^{-9}$ erg cm^{-2} s^{-1}. After that, the spectral parameters were compatible with the source

Table 3. Cut-off power-law best-fit parameters for the periods reported in Table 2.

Time (MJD[a])	INTEGRAL Observations (Rev. #)	Γ	E_c (keV)	χ^2_{red} (d.o.f.)	P^b
217.7–217.8	N.A.	$1.56^{+0.08}_{-0.05}$	$500_{-309}{}^{c}$	1.56 (280)	16
237.5–240.2	895	$1.29^{+0.47}_{-0.13}$	120^{+15}_{-12}	0.84 (97)	7
240.7–243.2	896	1.22 ± 0.06	105^{+12}_{-10}	1.06 (102)	2
243.7–246.2	897	$1.29^{+0.09}_{-0.08}$	125^{+34}_{-22}	0.75 (103)	2
246.7–249.1	898	$1.30^{+0.05}_{-0.06}$	111^{+14}_{-10}	1.18 (102)	5
249.7–252.1	899	1.30 ± 0.08	118^{+30}_{-18}	1.23 (102)	3
252.5–255.1	900	1.27 ± 0.08	108^{+25}_{-16}	0.77 (102)	2
255.6–258.1	901	1.39 ± 0.07	$134\ ^{+33}_{-23}$	1.02 (102)	10
259.9–261.1	902	1.69 ± 0.04	328^{+94}_{-64}	1.69 (333)	27
264.5–267.1	904	1.30 ± 0.04	88 ± 6	1.21 (102)	8
267.6–270.1	905	1.45 ± 0.07	116^{24}_{-17}	1.21 (102)	11
270.4–272.8	906	1.42 ± 0.07	$99\ ^{+17}_{-13}$	1.49 (102)	10
273.4–276.0	907	$1.47^{+0.07}_{-0.06}$	98^{+15}_{-11}	1.66 (102)	11
276.4–278.8	908	$1.46^{+0.07}_{-0.06}$	89^{+14}_{-10}	1.17 (102)	14
279.4–281.5	909	1.77 ± 0.04	183^{+28}_{-23}	0.92 (312)	15
281.7–281.8	N.A.	$1.68^{+0.10}_{-0.11}$	409^{c}_{-247}	1.49 (254)	14
282.4–284.9	910	$1.66^{+0.05}_{-0.04}$	126^{+17}_{-10}	1.53 (96)	4
289.3–289.6	N.A.	1.65 ± 0.01	500^{c}_{-48}	1.73 (227)	19
297.8–297.9	N.A.	1.91 ± 0.01	$500\ ^{c}_{-77}$	1.86 (259)	17
301.1–303.3	916	2.15 ± 0.03	$99\ ^{9}_{-7}$	1.69 (252)	61
303.6–303.8	N.A.	$1.93^{+0.08}_{-0.09}$	37^{+10}_{-7}	1.65 (192)	84
310.6–310.7	N.A.	$2.32^{0.06}_{-0.07}$	$500\ ^{c}_{-299}$	1.55 (177)	100

Notes. [a] MJD−55000. [b] Percentage of the disc flux versus the power-law flux. [c] Pegged at hard limit (500 keV).

changing from the LHS to the HIMS (until MJD ∼ 55303.6), then to softer states (to the SIMS until MJD 55304.7, then quickly to the SS, MJD ∼ 55306.1, and finally back to the SIMS and HIMS (see Fig. 3) around MJD 55320 (Motta et al. 2010b), but this is beyond the scope of our paper because it happened after the observations listed in our Tables.

3.4. Multi-wavelength studies

Observations at other wavelengths of GX 339−4 were conducted with *Swift*/UVOT from MJD ∼ 55280 to 55300 (Yu 2010), aimed at fast optical/UV variability in the hard state and transition. No rapid optical/UV variability was detected owing to the low UVOT count rates. Our long-term FTS optical light curves of this outburst are shown in Fig. 2. The source brightened by ∼4.5 mag in V-, R- and i'-bands from a low-luminosity state in 2009 October, MJD 55126 (Lewis & Russell 2009). GX 339−4 reached the brightest magnitudes recorded on 2010 April 1, MJD 55287 ($V = 15.05 \pm 0.02$; $R = 14.49 \pm 0.01$; $i' = 14.26 \pm 0.01$), just before the start of the transition from the LHS to softer states. During this LHS rise, the source brightened at a mean rate of ∼0.01 mag d^{-1} between MJD 55237–55287. There was considerable optical short-term variability in the LHS. From several consecutive exposures between MJD 55273–55320, we measured a fractional rms variability in the i' band that was fairly constant: ∼9–11% with typical errors of ∼1% (on each date, the time resolution was between 90 and 130 s). This short-term variability throughout the outburst, including the decay, will be detailed in another paper (Russell et al., in prep.). Our results are similar to the optical fractional rms previously reported at time resolutions of <1 s in the LHS of GX 339−4 (see, e.g., Gandhi et al. 2010). Between MJD 55294–55297, the optical flux faded rapidly by ∼1 mag in 3.0 days (Russell et al. 2010) and a change in the SED to a bluer colour was observed (see Sect. 4.2). At the same time the *Swift*/BAT flux started to fade, marking the beginning of the transition away from the LHS (Fig. 2). The rapid optical fading was also accompanied by a drop in the i'-band fractional rms variability to 1.3 ± 0.7% by MJD ∼ 55301. As the source continued to soften in X-rays (Fig. 3), the optical flux remained fairly constant in the following few months, around $V \sim 16.5$; $R \sim 16.0$ and $i' \sim 16.0$ mag, with an i'-band fractional rms of <5%. REM data showed that the source was basically at a constant luminosity on MJD 55260–55261 (during Rev. # 902) while on MJD 55303 (during Rev. # 916) the source faded consistently by a factor of ∼2 in the optical (V- and R-band) and by a factor of ≥5 in the NIR (I- and H-band), in agreement with the FTS results. Months later, after the peak of the outburst, the optical and NIR brightnesses in the V, R, I, J, H and K filters all decreased. A spectrum was taken with the ISAAC instrument on the ESO telescope between MJD 55261.3–55261.4 and

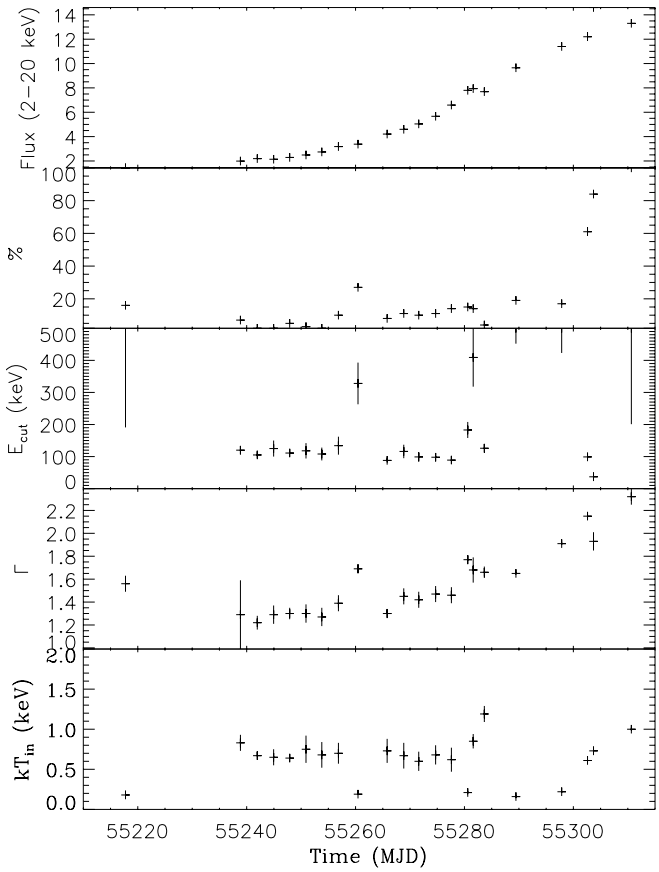

Fig. 6. Summary of the parameter evolutions of GX 339−4 along its outburst: 2–20 keV flux (10^{-9} erg cm^{-2} s^{-1}), % of disc versus power-law flux, high-energy cut-off energy (keV), corresponding photon index and inner disc temperature (keV). See Tables 2 and 3, and text for details.

MJD 55307.2–55307.2, and had a flux and spectral shape similar to our REM and FTS photometric data (Rahoui et al. 2011, in prep.).

The ATCA observations conducted on MJD 55283 showed flux densities ∼20 mJy with an inverted radio spectrum, with a spectral index in the range: +0.1 to +0.2, typical of powerful self-absorbed compact jets observed in the LHS. On MJD 55372, no radio emission was detected at the location of GX 339−4: this was consistent with the source being in a soft state (Corbel et al. 2010b). Ejecta very close to the core of the system were detected with a spectral index of -0.34 ± 0.08 (which is typical of optically thin synchrotron emission). The new radio source was in the same direction as the large-scale jets already detected in GX 339−4 (see Gallo et al. 2004): the impact of material ejected by the system into the ISM was observed (see the discussion below).

4. Discussion

4.1. Interpretations

According to Wu et al. (2010), this bright outburst should have peaked at >0.83 Crab in hard X-rays. This is based on the empirical relationship between the hard X-ray peak flux and the waiting time since the last bright (>0.12 Crab) outburst of GX 339−4. The source transited at almost the expected time and flux (see below); the softening of the X-ray flux at this transition occurred at a slightly lower flux than the 2002–2003 and 2007 outbursts, but at a brighter flux than the 2004–2005 outburst. The transition may have occurred slightly earlier because there were a few low-level LHS mini-outbursts between the 2007 and 2010 outbursts (Kong 2008; Markwardt 2009). These mini-outbursts could have emptied the disc a bit more than if the source was in true quiescence the whole time. The BAT, ISGRI, PCA and ASM light curves show that the hard X-rays were dominated by the power-law component while the soft X-rays were mainly caused by the disc (whose flux increased with time) plus the power-law (which was fading at the same time). When the power-law component returns, we observe the spectral transition back from soft into harder states, and a secondary peak in the hard X-rays. The outburst evolution of GX 339−4 during the 2010 episode is fairly typical of BH outbursts in general.

Our spectral analysis showed that the source transited from an initial LHS, with a spectrum dominated by Comptonisation in the beginning of the outburst (MJD ∼ 55217– 55281), to softer states where the power-law cut-off was not needed anymore and the photon index of the power-law was very soft (∼2.3). In X-ray binaries a cut-off power-law spectrum is usually interpreted as the signature of inverse Comptonisation of soft-seed photons by a thermalised (i.e., with velocities following a Maxwellian distribution) population of electrons. Changes in the hard component can signal the presence of a compact jet, a corona, or reprocessed hard X-ray emission caused by X-ray heating from an extended central source. The hard component therefore evolved as expected. Regardless of the caveats mentioned in Sect. 3.3 about the DISKBB components and the exact value of the inner radius obtained from the fits, we see a trend in the disc parameters (Table 2 and Fig. 6) that is compatible with an increase of the mass accretion rate before the transition. Then the disc on the whole recedes when the source reaches a low luminosity (see, e.g., Tomsick et al. 2009) during the decay phase of the outburst. Although we have then observed the disc slowly moving outwards during the hardening (Chen et al. 1997; Cadolle Bel et al. 2004), this is not necessarily true for all transient sources (see, e.g., Miller et al. 2006). This is still strongly debated (Done et al. 2007; Rykoff et al. 2007; Gierliński et al. 2008) as, for example, in XTE J1817−330. We do not address this question specifically in this work because the majority of our data were taken in the LHS and not long after the main transition into softer states. In addition, with a lower energy limit often at 3 keV, few data are sensitive enough for this purpose. However, one can remark that the fairy low disc temperatures are consistent with the compact object being a BH and not a neutron star (e.g., Tanaka & Lewin 1995). The soft and hard X-rays evolved as seen in previous outbursts of GX 339−4: first in the HIMS, the source transited to softer states where the disc dominated the emission, the inner disc moved closer to the BH and then gradually cooled down before returning to quiescence.

The spectral evolution is consistent with other works: RXTE monitoring showed softening and LFQPO evolutions (Shaposhnikov & Tomsick 2010; Motta et al. 2010a; Yu 2010) as GX 339−4 began to leave the LHS (Motta et al. 2010a). Figure 6 shows some differences with Fig. 6 of Motta et al. (2009): while the fluxes, disc temperature and power-law indices show the same trend, our individual cut-off values are sometimes very high (e.g., near MJD 55260), like in the HSS of their Fig. 6, and no cut-off is needed. The evolution in the rising phase of the LHS is therefore not as smooth as expected at higher energies (which are well constrained for the first time), but there is no clear explanation for that. The 2–20 keV flux (from 1.43 to 14.6×10^{-9} erg cm^{-2} s^{-1}) and the bolometric flux (extrapolated from 0.01 to 1000 keV) variations (0.82 to 2.93×10^{-8} erg cm^{-2} s^{-1}) confirm this spectral evolution. The source

reached a high luminosity at the maximum of $\sim 12.9 \times (\mathrm{d}/6\ \mathrm{kpc})^2$ 10^{37} erg s^{-1}. This represents ∼18% of the Eddington luminosity for a 7-solar-mass BH; stellar mass BHs accreting at or below 10^{-2} L_{Edd} are found in the LHS (McClintock & Remillard 2006). Additionally, the evolution of the reflection component from 0.19 to 0.51 indicates that the source became softer. After the observations presented in this paper, the source switched back to the SIMS, and subsequently to the HIMS. This is not unusual: during the decay of their outbursts, XTE J1720−318, XTE J1650−500 and *Swift* J1753.5−0127 showed a slowly receding disc with a decreasing inner temperature, while at the same time the relative amount of the power-law contribution increased again. A year after the beginning of its outburst (end of February 2011), GX 339−4 finally switched back to the LHS (Russell & Lewis 2011a), and then to quiescence (Russell & Lewis 2011b).

The broadband spectral parameter evolution from hard to soft states and our radio/NIR/optical studies are consistent with the preliminary results of Lewis et al. (2010) and Corbel et al. (2010a). A discrete radio ejection usually occurs around the hard-to-soft transition in a BH transient outburst: Corbel et al. (2010b) witnessed the interaction of a relativistic jet from GX 339−4 with the interstellar medium with the ATCA, implying that a major ejection occurred earlier. During the LHS we detected the compact core jet in the optical/IR. The source continued to rise in the LHS for a while (Wu et al. 2010), therefore it was also rising at radio frequencies. We added radio flux data to our SED (Fig. 8) but the entire campaign will be presented in a forthcoming paper (Corbel et al., in prep.). The rapid drop in optical flux and colour change observed at the start of the state transition are reminiscent of previous outbursts (Coriat et al. 2009). Because rapid variability probably originates in the synchrotron jet component (Casella et al. 2010; Gandhi et al. 2010), this indicates the jet no longer makes a strong contribution to the optical emission and that it was fading (Russell et al. 2010). This chromatic behaviour, also observed in the REM data, hints at a component that mainly contributes in the NIR frequencies, which then fades or disappears after the transition (see also Fig. 7). The optical and infrared flux continued to drop in the days following the transition. The changes in optical flux and spectrum over the transition have been reported before for GX 339−4 (Homan et al. 2005; Coriat et al. 2009) and other BH LMXBs (see, e.g., Buxton & Bailyn 2004; Russell et al. 2007). We clearly detected the jet evolution and its dramatic quenching at all wavelengths.

4.2. Spectral energy distributions

To compute the NIR/optical spectral energy distributions (SEDs) of the source, we first corrected our magnitudes for interstellar absorption. We assumed a colour excess of $E(B-V) = 1.2 \pm 0.1$ (Zdziarski et al. 1998), which is fully consistent with our measurements of N_{H} and of Corbel & Fender (2002). Using standard extinction curves from Fitzpatrick (1999) and Kataoka et al. (2008), we obtained the de-reddening parameters for each of our UV/optical/NIR filters (Table 4). Figure 7 was obtained with the FTS, SMARTS and REM data at four distinct epochs (see caption). The spectra clearly changed between the FT South and SMARTS epochs (MJD ∼ 55298).The jet faded over the transition and our last REM observations (MJD ∼ 55303), while the other component (probably the disc) stayed about the same. The *H*-band faded by a factor of 10 whereas, the *V*-band faded by a factor >2.5. The jet contribution moved to lower frequencies: data taken on MJD ∼ 55298 still have the jet dominating in the *H*-band in NIR, but no longer in the optical. The last SED is bluer according to Fig. 7. This is exactly what one can expect when a source undergoes an LHS to HSS spectral transition: the colour changed and thermal processes started to dominate. During the rising LHS, Gandhi et al. (2011) found that the jet spectrum was highly variable in the mid-IR. The break between optically thick (self-absorbed) and optically thin synchrotron emission in the jet spectrum was found to vary between ∼3.6 and 22 μm on timescales of minutes–hours. Here, we witness in Fig. 7 this jet component fading over timescales of days.

We produced broadband SEDs in two distinct spectral states (hard and soft), composed of simultaneous radio (when available), (de-reddened) UV/optical/NIR and unabsorbed X-ray/soft γ-ray data. They are shown in Figs. 8 and 9. In Fig. 8 we plot the data obtained during the first INTEGRAL ToO (MJD 55259.9–55261.1, Rev. # 902). Figure 8 is remarkably similar to the Fig. 2 of Corbel & Fender (2002), focusing on GX 339−4 jet

Table 4. De-reddening parameters used for the REM telescope, FTS and UVOT values.

Filter	λ_c (Å)	A_λ (mag)
REM- *V*	5505	3.64
R	6588	2.81
I	8060	2.04
J	12 500	0.96
H	16 500	0.62
K	21 600	0.42
FTS-*V*	5448	3.69
R	6407	2.92
i′	7545	2.27
UVOT-*uw*2	1928	9.74
*um*2	2246	10.97
*uw*1	2600	7.91
u	3465	5.93
b	4392	4.88
v	5468	3.67

Notes. We assumed $E(B-V) = 1.21 \pm 0.17$ mag to correct the UV/optical/NIR photometry of GX 339−4.

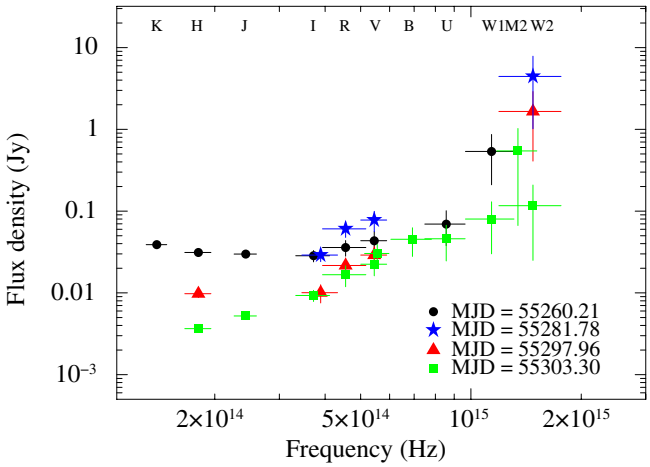

Fig. 7. Compiled SEDs with UVOT, REM, SMARTS (Buxton et al. 2011) and FTS data at distinct MJD: MJD = 55260.21 (UVOT/*uw*1, *u* and REM/*V*, *R*, *I*, *J*, *H*, *K*); MJD = 55281.78 (UVOT/*uw*2 and FTS/*V*, *R*, *i′*); MJD = 55297.96 (UVOT/*uw*2, FTS/*R*, *i′* and SMARTS/*V*, *H*) and MJD = 55303.30 (UVOT/*uw*2, *um*2, *uw*1, *u*, *b*, *v*, SMARTS/*V*, *I*, *J*, *H* and REM/*R*). The error bar is so large that the fluxes of *uw*1, *um*2 and *uw*2 are comparable (within the errors).

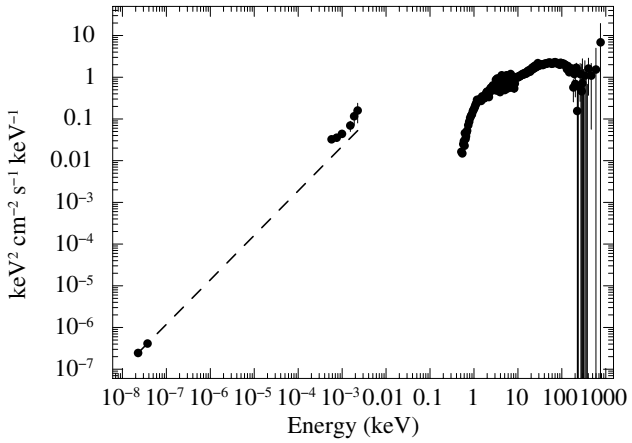

Fig. 8. SED from radio to soft γ-ray data plotted in flux (keV^2 × cm^{-2} × s^{-1} × keV^{-1}) versus energy (keV) at MJD ∼ 55259.9–55261.1 (Rev. # 902). It is remarkably similar to the Fig. 2 of Corbel & Fender (2002). The dashed line is a simple power-law extrapolation of the two radio data points up to the NIR frequencies (this is not a physical model, but only shown for visual purpose; see Sect. 4.2).

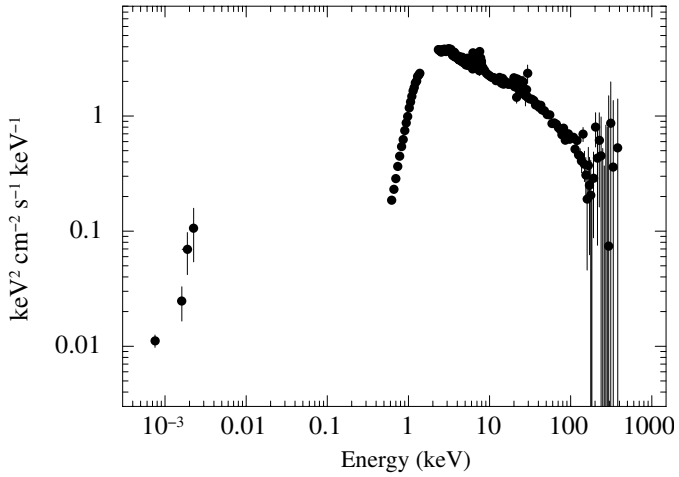

Fig. 9. SED from NIR to soft γ-ray data plotted in flux (keV^2 × cm^{-2} × s^{-1} × keV^{-1}) versus energy (keV) around MJD 55301.1–55303.3 (Rev. # 916).

signatures during LHS. One can interpret the results with simple power-laws, but note that this is a very rough approach and not a physical model. An extrapolation of the radio data up to the NIR/optical clearly does not fit the data. Excess NIR/optical emission is observed. Possible sources of the residual emission are the disc, the irradiated face of the companion star (because the companion cannot contribute much, see Shahbaz et al. 2001; Hynes et al. 2004) and the jets. Similarly, several power-law components with distinct slopes are needed to fit our SEDs.

For example, using a simple, double power-law fit to the data in Fig. 7 yields indices of −0.9 ± 0.4 for the NIR range. We fixed the optical component (where the disc is assumed to dominate) to 1.7, which is the value we found fitting a single power-law to our SED around MJD 55303, where the jet contribution was absent or still negligible (thus assuming that at that epoch, we only have contribution from the disc). For this SED in the soft state (Fig. 9) we observed significant spectral changes both in the disc and hot medium components and found that a simple single power-law model was sufficient to fit the UV/optical/NIR data (Fig. 7), with an index of 1.7 ± 0.2. This indicates the fading jet component in GX 339−4, as previously

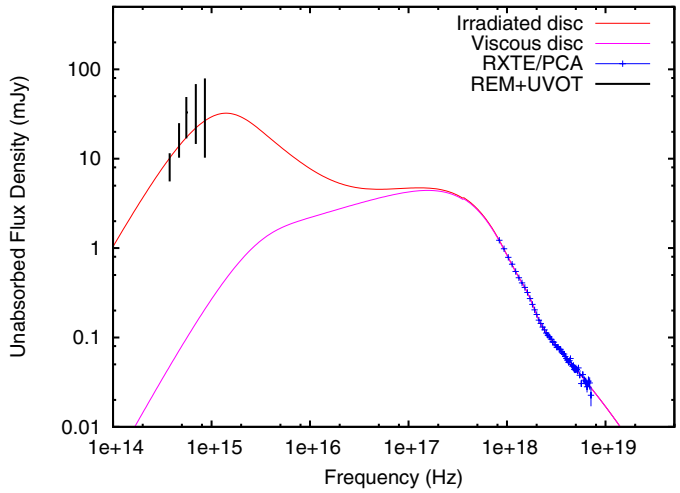

Fig. 10. Unabsorbed flux density (in mJy) versus frequency (Hz) from the RXTE (violet), REM and UVOT (black) data of GX 339−4 fitted with a Gaussian, a Comptonisation model plus 1) an irradiated disc (red) or 2) a viscous disc (pink) around MJD 55303.6–55303.8. The irradiated disc fits the data better (see Sect. 4.2).

discussed. The NIR/optical ESO/ISAAC spectroscopy taken at that time will be commented on in a forthcoming paper (Rahoui et al., in prep.).

After the LHS the radio spectral index became typical of optically thin synchrotron radiation, probably as a result of freely expanding plasma blobs previously ejected (see, e.g., Fender et al. 2004). This suggests that multiple ejection events took place during the outburst of GX 339−4 and then interacted with the interstellar medium, see Corbel et al. (2010b). This could potentially result in re-acceleration of particles up to very high energies. In general, the shape of our SEDs during the LHS are similar to the ones of the transient LMXB XTE J1118+480 (Chaty et al. 2003; Zurita et al. 2006): in its 2000 outburst, the SED from radio to X-rays has been explained as a combination of synchrotron radiation from a jet and a truncated optically thick disc, whereas models assuming advection dominated accretion flows alone underestimated the optical and IR fluxes (Zurita et al. 2006, and references therein). Discrepancies observed between the optical and IR SEDs of XTE J1118+480 in 2005 suggested that the IR was dominated possibly by a jet, whereas the optical was dominated by disc emission. Power-law fits to optical SEDs have also been performed for other BH XTs in outburst (Hynes 2005). All optical SEDs exhibit quasi power-law spectra, with α ranging from 0.5–1.5, all steeper than that expected for a viscously heated, multi-temperature disc: $S_\nu \propto \nu^{1/3}$ (which differs from our value taken closer to the peak). Also, the authors found for these BHs that the UV/optical/X-ray data – when detected – could be fitted with a simple black-body model of an accretion disc heated by internal viscosity and X-ray irradiation, but the inner radius could not be adequately constrained. They concluded that the flat-spectrum synchrotron emission may be important in the IR and optical in this source. However, they did not exclude the alternative explanation that the IR excess could come from the cool outer disc. More recently, Russell et al. (2011) even showed in the colour-magnitude diagram of XTE J1550−564 (Fig. 1 of their paper) that α can change dramatically over state transitions. In our observations of GX 339−4 presented here, the contribution of the radio to synchrotron emission up to the NIR/optical is significant, and we saw it fading over the transition (see Sect. 4.1). However, another component,

for example from the cooling disc and/or the irradiated companion, and/or an irradiated disc (van Paradijs & McClintock 1994; Hynes 2005) might be necessary to account for the NIR/optical excess observed. Note that in quiescence, the NIR/optical of GX 339−4 is likely dominated by an optically thin disc plus a much fainter mass donor star (Shahbaz et al. 2001).

Finally, we had sufficient NIR and optical data to ascertain when GX 339−4 was in the soft state and constructed the corresponding SED around MJD 55303.7 (Fig. 10). In fitting the SED, we used a technique similar to the one described in Rahoui et al. (2010): we tested a model consisting of a DISKIR (Gierliński et al. 2008; Gierliński et al. 2009) added to a GAUSSIAN, versus a model consisting of: DISKBB + GAUSSIAN + COMPTT. We fixed kT_e to the temperature found in Table 2. We found optical slopes around 2, which are consistent with thermal radiation. The reprocessing levels in the disc would need to be very high to explain the observed UV and optical fluxes. Our results are consistent with Coriat et al. (2009) as they fit SEDs with a reprocessing model and found a peak-temperature in the UV, where the maximum irradiation is expected. However, we can not constrain the parameters very well (in fact, they are underestimated) with photometry alone.

5. Conclusions

We obtained a unique data set with the most comprehensive collection of multi-wavelength data collected so far simultaneously for an outburst of GX 339−4 . We presented light curves and spectral evolution of GX 339−4 in outburst from hard to soft states. We confirmed that the broadband behaviour was consistent with previous outbursts, though some peculiarities were seen at high energies. Hynes' (2005) results on SEDs show a similar behaviour for a collection of BHs (see also, e.g., Russell et al. 2006, 2007). Extrapolating radio data to higher frequencies in the LHS SED might be interpreted as non-thermal emission from ejected material, such as discrete ejection events that rapidly faded. Jet emission contributed significantly to the radio, NIR and optical data. An optical excess was observed above the jet component and was explained by possible contributions from the disc (the companion cannot account much for the emission because it is fainter than $R > 21$ mag). However, alternative processes, such as X-ray irradiation, are sometimes inferred, depending on the source and available data. We now know that the amount of irradiation in NIR/optical varies depending on the luminosity and the X-ray state, as seen in our Fig. 10 around MJD 55303.7. We did not observe the source switching back to the LHS as we did for XTE J1720−318 (Cadolle Bel et al. 2004) or XTE J1817−330 (Cadolle Bel et al. 2008). For the first time, we have caught the jet quenching over the transition in many wavebands (Fig. 7). This provides an observational constraint on how the jet evolved over the outburst.

Acknowledgements. We thank the referee for his/her helpful comments that improved our manuscript. We thank the INTEGRAL, *Swift* and RXTE mission planners for programming the ToO observations described in the paper. The present work is partly based on observations with INTEGRAL, and ESA project with instruments and science data centre funded by ESA member states (especially the PI countries: Denmark, France, Germany, Italy, Switzerland, Spain), and Poland, and with the participation of Russia and the USA, and on observations with RXTE. The NRAO is a facility of the National Science Foundation operated under cooperative agreement by Associated Universities, Inc. M.C.B. acknowledges support from the Faculty of the European Space Astronomy Center (ESAC) and L. Prat's comments. JR acknowledges partial funding from the European Community's Seventh Framework Programme (FP7/2007-2013) under grant agreement number ITN 215212 "Black Hole Universe". JAT acknowledges partial support from NASA under *Swift* Guest Observer grant NNX08AW35G. The FT North and South are maintained and operated by Las Cumbres Observatory Global Telescope Network. This research has made use of the NASA Astrophysics Data System Abstract Service and of the SIMBAD database, operated at the CDS, Strasbourg, France.

References

Arnaud, K. A. 1996, ASP Conf., 101, 17
Belloni, T., Homan, J., Casella, P., et al. 2005, A&A, 440, 207
Belloni, T., Méndez, M., & Sánchez-Fernández, C. 2001, A&A, 372, 551
Belloni, T. M. 2010, Lect. Not. Phys. (Berlin: Springer Verlag), ed. T. Belloni, 794, 53
Bertin, E., & Arnouts, S. 1996, A&AS, 117, 393
Buxton, M., Dincer, T., Kalemci, E., & Tomsick, J. 2010, The Astronomer's Telegram, 2549, 1
Buxton, M., et al. 2011, AJ, submitted
Buxton, M. M., & Bailyn, C. D. 2004, ApJ, 615, 880
Cabanac, C., Fender, R. P., Dunn, R. J. H., & Körding, E. G. 2009, MNRAS, 396, 1415
Cadolle Bel, M., Rodriguez, J., Sizun, P., et al. 2004, A&A, 426, 659
Cadolle Bel, M., Sizun, P., Goldwurm, A., et al. 2006, A&A, 446, 591
Cadolle Bel, M., Kuulkers, E., Barragán, L., et al. 2008, Proc. A Population Explosion, St Petersburg/FL, USA, 28 Oct.–02 Nov. 2007
Cadolle Bel, M., Prat, L., Rodriguez, J., et al. 2009, A&A, 501, 1
Cadolle Bel, M., Kuulkers, E., Ibarra, A., et al. 2010, The Astronomer's Telegram, 2573, 1
Casella, P., Maccarone, T. J., O'Brien, K., et al. 2010, MNRAS, 404, L21
Chaty, S., Haswell, C. A., Malzac, J., et al. 2003, MNRAS, 346, 689
Chen, W., Shrader, C. R., & Livio, M. 1997, ApJ, 491, 312
Chincarini, G., Zerbi, F., Antonelli, A., et al. 2003, The Messenger, 113, 40
Corbel, S., & Fender, R. P. 2002, ApJ, 573, L35
Corbel, S., Fender, R. P., Tzioumis, A. K., et al. 2000, A&A, 359, 251
Corbel, S., Nowak, M. A., Fender, R. P., Tzioumis, A. K., & Markoff, S. 2003, A&A, 400, 1007
Corbel, S., Broderick, J., Brocksopp, C., Tzioumis, T., & Fender, R. F. 2010a, The Astronomer's Telegram, 2525, 1
Corbel, S., Broderick, J., Calvelo, D., et al. 2010b, The Astronomer's Telegram, 2745, 1
Coriat, M., Corbel, S., Buxton, M. M., et al. 2009, MNRAS, 400, 123
Covino, S., Stefanon, M., Sciuto, G., et al. 2004, in SPIE Conf. Ser. 5492, ed. A. F. M. Moorwood, & M. Iye, 1613
Done, C., Gierliński, M., & Kubota, A. 2007, A&AR, 15, 1
Fender, R. P., Belloni, T. M., & Gallo, E. 2004, MNRAS, 355, 1105
Fender, R. P., Homan, J., & Belloni, T. M. 2009, MNRAS, 396, 1370
Fitzpatrick, E. L. 1999, PASP, 111, 63
Frank, J., King, A., & Raine, D. J. 2002, Accretion Power in Astrophysics: 3rd ed., ed. Frank, J., King, A., & Raine, D. J. (Cambridge Univ. Press), 21
Gallo, E., Fender, R. P., & Pooley, G. G. 2003, MNRAS, 344, 60
Gallo, E., Corbel, S., Fender, R. P., Maccarone, T. J., & Tzioumis, A. K. 2004, MNRAS, 347, L52
Gallo, E., Fender, R. P., Miller-Jones, J. C. A., et al. 2006, MNRAS, 370, 1351
Gandhi, P., Dhillon, V. S., Durant, M., et al. 2010, MNRAS, 407, 2166
Gandhi, P., Blain, A. W., Russell, D. M., et al. 2011, ApJ, 740, L13
Gierliński, M., Done, C., & Page, K. 2008, MNRAS, 388, 753
Gierliński, M., Done, C., & Page, K. 2009, MNRAS, 392, 1106
Grove, J. E., Johnson, W. N., Kroeger, R. A., et al. 1998, ApJ, 500, 899
Homan, J., & Belloni, T. 2005, Astrophys. Space Sci., 300, 107
Homan, J., Buxton, M., Markoff, S., et al. 2005, ApJ, 624, 295
Hynes, R. I. 2005, ApJ, 623, 1026
Hynes, R. I., Steeghs, D., Casares, J., Charles, P. A., & O'Brien, K. 2003, ApJ, 583, L95
Hynes, R. I., Steeghs, D., Casares, J., Charles, P. A., & O'Brien, K. 2004, ApJ, 609, 317
Jahoda, K., Markwardt, C. B., Radeva, Y., et al. 2006, ApJS, 163, 401
Jordi, K., Grebel, E. K., & Ammon, K. 2006, A&A, 460, 339
Kalberla, P. M. W., Burton, W. B., Hartmann, D., et al. 2005, A&A, 440, 775
Kataoka, J., Madejski, G., Sikora, M., et al. 2008, ApJ, 672, 787
Kong, A. K. H. 2008, The Astronomer's Telegram, 1588, 1
Kuulkers, E., Shaw, S. E., Paizis, A., et al. 2007, A&A, 466, 595
Landolt, A. U. 1992, AJ, 104, 372
Laurent, P., & Titarchuk, L. 2007, ApJ, 656, 1056
Laurent, P., Rodriguez, J., Wilms, J., et al. 2011, Science, 332, 438
Lewis, F., & Russell, D. M. 2009, The Astronomer's Telegram, 2270, 1
Lewis, F., Russell, D. M., & Cadolle Bel, M. 2010, The Astronomer's Telegram, 2459, 1
Lewis, F., Russell, D. M., Fender, R. P., Roche, P., & Clark, J. S. 2008, ArXiv e-prints

Markoff, S., Nowak, M. A., & Wilms, J. 2005, ApJ, 635, 1203
Markwardt, C. B. Markwardt, N., Shaposhnikov, J. H. et al. 2009, The Astronomer's Telegram, 1945, 1
McClintock, J. E., & Remillard, R. A. 2006, Black hole binaries, Compact stellar X-ray sources, ed. W. Lewin, & M. van der Klis (Cambridge University Press), 157
Miller, J. M., Homan, J., Steeghs, D., et al. 2006, ApJ, 653, 525
Mitsuda, K., Inoue, H., Koyama, K., et al. 1984, PASJ, 36, 741
Motta, S., Belloni, T., & Homan, J. 2009, MNRAS, 400, 1603
Motta, S., Belloni, T., & Muñoz Darias, T. 2010a, The Astronomer's Telegram, 2545, 1
Motta, S., Belloni, T., Muñoz-Darias, T., & Homan, J. 2010b, The Astronomer's Telegram, 2593, 1
Muñoz-Darias, T., Casares, J., & Martínez-Pais, I. G. 2008, MNRAS, 385, 2205
Poole, T. S., Breeveld, A. A., Page, M. J., et al. 2008, MNRAS, 383, 627
Prat, L., Cadolle Bel, M., Terrier, R., et al. 2010, The Astronomer's Telegram, 2455, 1
Rahoui, F., Chaty, S., Rodriguez, J., et al. 2010, ApJ, 715, 1191
Rodriguez, J., Shaw, S. E., Hannikainen, D. C., et al. 2008, ApJ, 675, 1449
Roming, P. W. A., Kennedy, T. E., Mason, K. O., et al. 2005, Space Sci. Rev., 120, 95
Russell, D. M., & Lewis, F. 2011a, The Astronomer's Telegram, 3191, 1
Russell, D. M., & Lewis, F. 2011b, The Astronomer's Telegram, 3383, 1
Russell, D. M., Fender, R. P., Hynes, R. I., et al. 2006, MNRAS, 371, 1334
Russell, D. M., Fender, R. P., & Jonker, P. G. 2007, MNRAS, 379, 1108
Russell, D. M., Buxton, M., Lewis, F., & Altamirano, D. 2010, The Astronomer's Telegram, 2547, 1
Russell, D. M., Maitra, D., Dunn, R. J. H., & Fender, R. P. 2011, MNRAS, 416, 2311
Rykoff, E. S., Miller, J. M., Steeghs, D., & Torres, M. A. P. 2007, ApJ, 666, 1129
Shahbaz, T., Fender, R., & Charles, P. A. 2001, A&A, 376, L17
Shaposhnikov, N., & Tomsick, J. A. 2010, The Astronomer's Telegram, 2523, 1
Tanaka, Y., & Lewin, W. H. G. 1995, in X-ray Binaries, ed. Lewin, van Paradijs, & van den Heuvel (Cambridge University Press), 126
Tanaka, Y., & Shibazaki, N. 1996, ARA&A, 34, 607
Titarchuk, L. 1994, ApJ, 434, 570
Tomsick, J. A. 2010, The Astronomer's Telegram, 2384, 1
Tomsick, J. A., Yamaoka, K., Corbel, S., et al. 2009, ApJ, 707, L87
van Paradijs, J., & McClintock, J. E. 1994, A&A, 290, 133
Wilms, J., Allen, A., & McCray, R. 2000, ApJ, 542, 914
Wu, Y. X., Yu, W., Yan, Z., Sun, L., & Li, T. P. 2010, A&A, 512, A32
Yamaoka, K., Sugizaki, M., Nakahira, S., et al. 2010, The Astronomer's Telegram, 2380, 1
Yu, W. 2010, The Astronomer's Telegram, 2556, 1
Zdziarski, A. A., Poutanen, J., Mikolajewska, J., et al. 1998, MNRAS, 301, 435
Zdziarski, A. A., Gierliński, M., Mikołajewska, J., et al. 2004, MNRAS, 351, 791
Zerbi, F. M., & The Rem Team. 2001, in Astronomische Gesellschaft Meeting Abstracts, ed. E. R. Schielicke, J101
Zurita, C., Torres, M. A. P., Steeghs, D., et al. 2006, ApJ, 644, 432